

# Spatiotemporal Feature Alignment and Weighted Fusion in Collaborative Perception Enabled by Network Synchronization and Age of Information

Qiaomei Han, *Member, IEEE*, Xianbin Wang, *Fellow, IEEE*, Minghui Liwang, *Member, IEEE*, and Dusit Niyato, *Fellow, IEEE*

**Abstract**—Collaborative perception in Internet of Vehicles (IoV) aggregates multi-vehicle observations for broader scene coverage and improved decision-making. However, fusion quality degrades under spatiotemporal heterogeneity from unsynchronized clocks, communication delays, and motion variations across vehicles. Prior work mitigates these through spatial transformations or fixed time-offset corrections, overlooking time-varying clock drifts and delays that cause persistent feature misalignment. To overcome these, we propose a spatiotemporal feature alignment and weighted fusion framework. Specifically, network synchronization is designed to continuously compensate for clock state differences between vehicles and establish a common time reference, onto which all feature timestamps can be mapped. After synchronization, to align the freshness of received features since their generation, their **Age of Information** (AoI) is determined by estimating network delay with given feature size and link quality. Our spatiotemporal feature alignment then projects vehicles’ features into one spatial coordinate and corrects them to a synchronized fusion instant using AoIs, enabling all features to describe the scene coherently. Furthermore, due to varying synchronization and alignment quality, we estimate their uncertainties and integrate with AoI to generate feature weights for efficient fusion, prioritizing fresh, reliable feature regions. Simulations show consistent perception accuracy improvements over strong baselines under clock drifts and link delays.

**Index Terms**—Collaborative perception, Age of Information, spatiotemporal feature alignment, weighted fusion.

## I. INTRODUCTION

The proliferation of big data and widespread adoption of smart devices have driven rapid advancements in collaborative computing paradigm for enhanced decision-making capabilities and computational efficiency [1]. This paradigm has given rise to a wide variety of techniques including federated learning [2], split learning [3], and transfer learning [4], which allow distributed nodes to process local data and exchange knowledge across interconnected systems. By iteratively refining a shared global model, collaborative computing has propelled rapid progress in diverse domains, including smart manufacturing, smart cities, and smart healthcare [5], [6].

Building on this paradigm, collaborative perception aggregates observations from multiple vehicles for a broader and more accurate view of the environment, improving decision-making in Internet of Vehicles (IoV) [7]–[9]. Recent work increasingly targets feature-level collaboration, in which vehicles exchange compact, perception-oriented representations,

such as features summarizing the presence, position, and range of nearby road users around detected regions. Relative to object-level collaborative perception, which discards valuable surrounding contexts, and raw-level collaboration, which preserves detail at the cost of prohibitive bandwidth and latency, feature-level collaboration strikes a balance between content information and communication cost, which is accordingly adopted as the foundation of our framework.

Despite its potential, feature-level collaborative perception often suffers from spatiotemporal feature misalignment across different vehicles. Temporal feature misalignment stems from imperfect clock synchronization and varying communication delays [10], [11], whereas spatial feature misalignment arises from discrepancies in each vehicle’s coordinate system, so that these vehicles’ features are produced at different instants and from distinct positions and viewpoints; directly aggregating them is ineffective and ultimately degrades the perception fusion accuracy [12]–[14].

To mitigate feature misalignment, most existing algorithms primarily address spatial domain variation. They transform features from different vehicles into a common coordinate system using techniques such as rotation, translation, or learned geometric mappings [15], [16]. Although these methods substantially reduce motion- and viewpoint-induced discrepancies, they rectify geometry only at a single timestamp, leaving temporal feature inconsistency unaddressed. Consequently, residual time offsets persist and manifest as apparent spatial domain drift over time, undermining the alignment accuracy in dynamic scenes.

Beyond purely spatial feature alignment, recent work has begun to address temporal feature compensation. SyncNet [17] predicts the current feature map from past inputs under a uniformly sampled delay model. CoBEVFlow [18] estimates a Bird’s-Eye-View (BEV) flow field to warp asynchronous features to the receiver’s fusion time, accommodating irregular timestamps. However, they typically assume identical clocks and synchronized operation across perception stages. However, each stage, from feature extraction to fusion, introduces time-varying latency even on a single vehicle, and cross-vehicle operation compounds these delays due to clock drift or communication delay, leaving residual temporal misalignments and accumulating into spatial discrepancies as scenes evolve. Without explicitly accounting for such residual discrepancies, the fusion process lacks a reliability signal to modulate feature fusion weights, allowing stale or misaligned regions to be

treated nearly equally with well-aligned ones and thereby degrading perception under fast motion or fluctuating link conditions [12]–[14].

Furthermore, to improve collaborative perception efficiency, Region-of-Interest (RoI)-level weighted fusion focuses attention on most informative regions while avoiding the processing of full feature maps [19], [20]. Recent studies prioritize these RoIs by their freshness, quantified via Age of Information (AoI) [21], [22]. A critical limitation, however, arises from how AoI is computed. Existing methods derive freshness from the estimated network delay, which relies on feature size and link quality but ignores the unsynchronized clocks between vehicles. Consequently, the computed AoI conflates the true network delay with unknown inter-vehicle clock offset, which may lead to a feature appearing fresh to the sender but stale to the receiver, rendering AoIs from different vehicles incomparable. To resolve this, AoI should be referenced to a synchronized time base anchored at the fusion moment, and coupled with an uncertainty estimate that captures residual synchronization and alignment errors. After that, integrating both AoI and uncertainty to generate fusion weights will enable fresh, reliable RoIs to be prioritized, while ensuring efficient perception under dynamic scenes and link conditions.

Motivated by these considerations, we propose a framework for spatiotemporal feature alignment and weighted fusion by network synchronization and AoI. Our main contributions are:

- To establish an accurate temporal reference, we design network synchronization to estimate and update inter-vehicle clock states continuously. This allows local feature timestamps to be mapped onto a unified synchronized temporal reference. On this basis, AoI for each feature is computed by estimating network delay from its size and link quality since generation. Unlike fixed time-offset approaches, this method provides a precise measure of feature freshness, enabling effective fusion under clock drifts and network delays.
- Building upon the synchronized temporal reference, a spatiotemporal feature alignment mechanism is proposed. Features from different vehicles are projected into a common spatial coordinate system. A temporal compensator, conditioned on AoI, then corrects misalignments caused by time difference. Throughout the synchronization and alignment process, both time-induced and purely spatial uncertainties are modelled and converted into a reliability metric, for guiding downstream feature fusion.
- To maintain communication and computation efficiency, we perform the RoI-level weighted fusion, where AoI and reliability jointly determine the fusion weights. This strategy prioritizes fresh and reliable regions while down-weighting stale or uncertain ones. Compared to uniform or confidence-only fusion schemes, our weighting mechanism enhances perception accuracy and efficiency, particularly under dynamic scenes and link conditions.
- Our proposed framework is trained end-to-end and optimized towards both alignment and fusion objectives. In multi-vehicle simulations with clock drifts and communication delays, our approach consistently outperforms strong baselines in perception accuracy while maintaining

high efficiency. These results validate the effectiveness of the proposed framework in improving decision-making for IoV applications.

The remainder of this article is organized as follows: Section II reviews the related work on spatiotemporal feature alignment and weighted fusion in collaborative perception. Section III describes our proposed spatiotemporal feature alignment and weighted fusion framework by network synchronization and AoI. To evaluate its effectiveness, Section IV demonstrates simulation results. Finally, Section V concludes the paper and proposes future directions.

## II. RELATED WORK

In this section, we review some existing work related to feature alignment and fusion, overcoming the challenges arised from spatiotemporal data heterogeneity and unselected fusion.

### A. Spatiotemporal Feature Alignment

Due to spatiotemporal heterogeneity across vehicles caused by unsynchronized clocks, network delays, or motion discrepancies, the quality of collaborative perception is degraded. Early approaches mainly mitigate *spatial* feature misalignment by projecting features or detections into a common coordinate system via rigid rotations, translations or by warping BEV grids to compensate for viewpoint changes. NEAT [23] predicts feature-level corrections prior to fusion, improving robustness to pose noise. Vehicle-to-Everything (V2X)-ViT [16] applies an attention mechanism to aggregate cross-agent information, effectively learning where and how to fuse. These designs reduce geometric mismatch but presume synchronous inputs; when agents are time-shifted by latency or clock drift, they cannot eliminate the *temporal* misalignment.

Another line of work targets *temporal* feature misalignment. For example, SyncNet [17] forecasts the current feature map from past inputs under a uniformly sampled delay model, assuming homogeneous clock parameters across vehicles and stage-wise synchronization from feature extraction through fusion. However, each perception stage incurs time-varying latency even on a single vehicle, and cross-vehicle operation compounds this, causing temporal gaps to remain unaddressed and accumulate into spatial domain misalignments as scenes evolve. CoBEVFlow [18] estimates a BEV flow field to warp sender features from their native timestamps to the receiver's fusion time, accommodating irregular timestamps. However, it assumes perfectly synchronized clocks, making it vulnerable to residual errors from clock drift and imperfect alignment. As a result, even aligned features can gradually deviate, diminishing the effectiveness of performance improvement.

Therefore, the above observations surface two unmet requirements: (i) a *shared temporal reference* that makes feature freshness comparable across vehicles; and (ii) an *uncertainty quantification* tied to synchronization and alignment, allowing fusion to discount stale or misaligned updates. To address these gaps, we estimate inter-vehicle clock states and compute AoI with respect to the fusion-time reference, then propagate synchronization and alignment uncertainties attached to each aligned feature, yielding sustained perception accuracy under dynamic scenes and variable link conditions.

### B. Weighted Feature Fusion

For communication efficiency, many collaborative perception systems prioritize the most informative regions rather than full feature maps. *Where2comm* [20] learns a spatial confidence map to select critical areas and adapt communication to bandwidth, yielding minimal accuracy loss. *When2com* [24] jointly learns when to transmit and how to form communication groups, while *Who2com* [19] uses a multi-stage handshake to decide from whom to request information when the local view degrades. These methods design a filter-then-fuse paradigm driven primarily by spatial or semantic contexts. Challenges arise from the lack of an accurate temporal reference and its corresponding uncertainty quantification.

Information freshness, measured by AoI, quantifies the elapsed time between a sample's generation at the source and its observation at the receiver [21], [25]. In collaborative perception, methods such as *Fresh2Comm* [22] exploit AoI in weighted fusion to prioritize recent inputs. However, these approaches assume a common temporal reference, while clock offsets and variable link delays cause vehicle-local AoI values to be incomparable, leading to misprioritized fusion. To overcome this, we compute AoI on a shared, synchronized timeline and augment it with an uncertainty estimate reflecting residual synchronization and alignment errors, allowing the fusion process to favor features that are both fresh and reliable.

### III. A SPATIOTEMPORAL FEATURE ALIGNMENT AND WEIGHTED FUSION FRAMEWORK

For collaborative perception in IoV systems [26], [27], perception accuracy and efficiency are often hindered by spatiotemporal feature misalignment and unselected feature sharing, as shown in Fig. 1, leading to degraded perception quality and efficiency. To address these, we introduce a framework that augments perception features with a spatiotemporal correction and an ROI-level weighted fusion for improving perception accuracy and efficiency.

#### A. Preliminaries

1) *System Model*: We consider an IoV system comprising a set of vehicles  $\mathcal{M} = \{1, \dots, M\}$ . Each vehicle is equipped with an onboard unit that supports computation and wireless communication. A Roadside Unit (RSU), which integrates an edge server and a base station (BS), operates within the coverage area to coordinate collaboration. To characterize the remaining distance of the  $m$ -th vehicle before it leaves the RSU coverage, we define

$$d_m = \sqrt{\psi_r^2 - \psi_v^2} - \frac{v_m}{|v_m|} \psi_m, \quad (1)$$

where  $\sqrt{\psi_r^2 - \psi_v^2}$  is the half-length of the RSU's coverage along the road,  $\psi_m$  is the vehicle's position along the road axis, and  $v_m/|v_m|$  indicates its driving direction. Based on this, we define  $L = \{l \mid \|\psi_l - \psi_m\| \leq \iota\}$  as the set of neighboring vehicles within distance  $\iota$  of vehicle  $m$ .

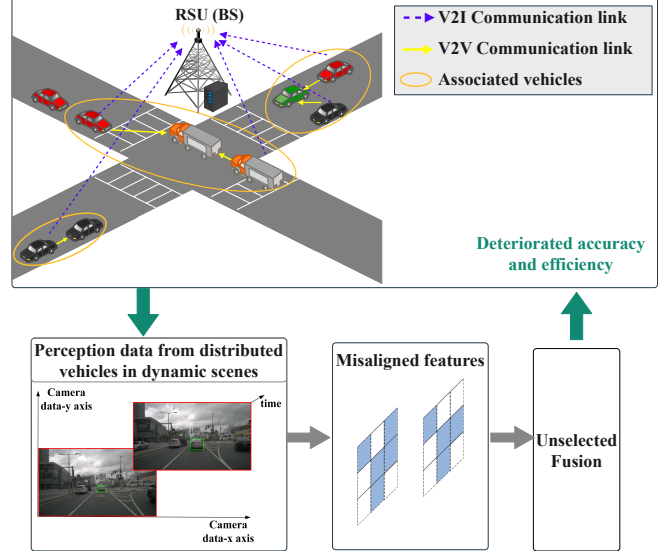


Fig. 1: Collaborative perception impacted by spatiotemporal feature misalignment and inefficient feature fusion.

2) *Feature Extraction*: For vehicle  $m$ , it collects point-cloud data from its LiDAR sensor as

$$\mathbf{X}_m = \{X_m^{(x,y,z,i)} \mid i = 1, 2, \dots\}, \quad (2)$$

where each element  $X_m^{(x,y,z,i)}$  means the 3D coordinates  $(x, y, z)$  of the  $i$ -th point. These points are processed by an encoder  $\Phi_{\text{enc}}(\cdot)$  to produce a feature tensor [26]

$$\mathbf{F}_m = \Phi_{\text{enc}}(\mathbf{X}_m). \quad (3)$$

Here, a voxel-based PointPillars model [28] is used for encoding, which outputs  $\mathbf{F}_m \in \mathbb{R}^{X \times Y \times Z \times C}$ , where  $X \times Y$  is the ground-plane BEV grid,  $Z$  is vertical resolution, and  $C$  is the number of feature channel.

Based on these extracted features, we introduce a spatiotemporal feature alignment and weighted fusion framework, as shown in Fig. 2, which comprises three stages. (i) Network synchronization establishes a common temporal reference across vehicles. On this basis, AoI is computed for each vehicle's features at the fusion instant. (ii) Spatiotemporal feature alignment geometrically warps neighbor features into the ego vehicle's coordinate and uses AoIs to temporally compensate them. (iii) Weighted fusion assigns ROI-level weights as a joint function of AoI and uncertainty-derived reliability, prioritizing fresh and reliable feature regions for fusion.

#### B. Network Synchronization

Without accurate synchronization, any two vehicles could timestamp the same event differently, leading to mismatched or stale feature fusion that degrades perception performance. Thus, we build a common temporal reference between ego vehicle  $m$  and each neighbor  $l \in L$ , and track the uncertainty of the built reference for downstream feature fusion.

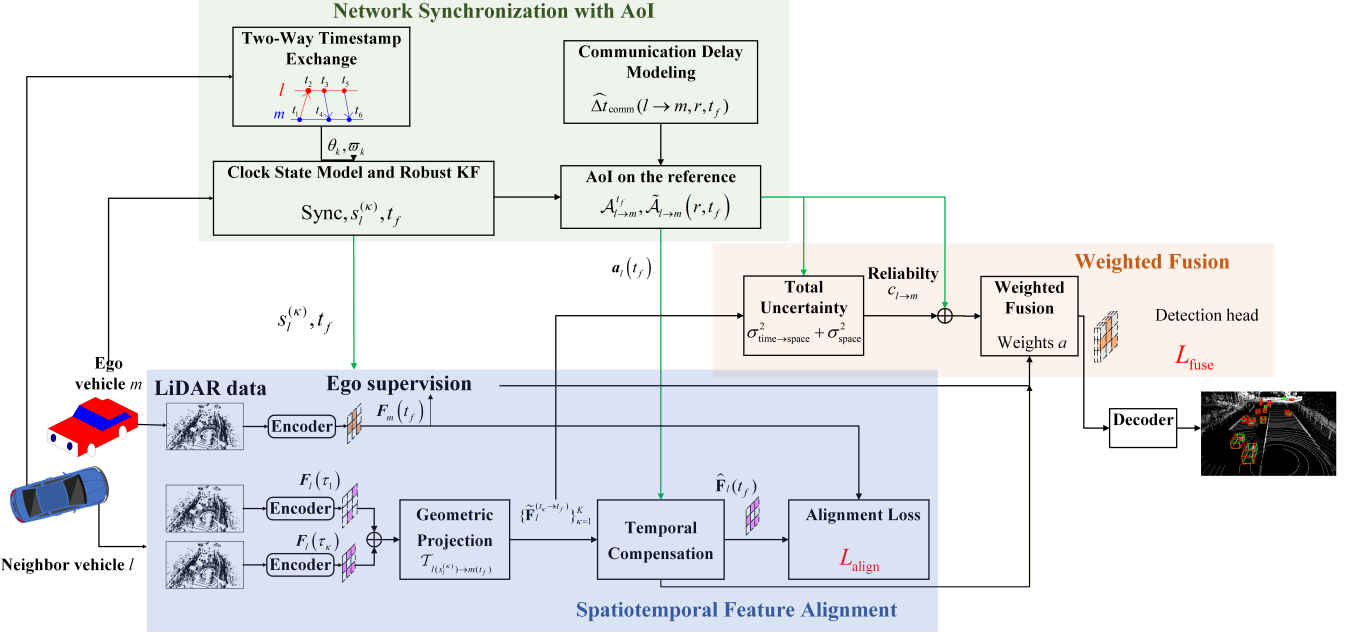


Fig. 2: Workflow of our proposed framework for collaborative perception, including network synchronization, spatiotemporal feature alignment, and weighted feature fusion.

1) *Two-Way Timestamp Exchange*: The ego vehicle first establishes its clock relations with each neighbor, including capturing both clock offset and skew parameters. To achieve this, a two-way timestamp exchange protocol, IEEE 1588 Precision Time Protocol (PTP), is adopted [10].

At the  $k$ -th round of message exchange ( $k \in K$ ), the ego vehicle  $m$  and a neighbor  $l \in L$  perform a bidirectional message exchange, which yields six timestamps:

- $m$  sends a Sync message to  $l$  at time  $t_{1,k}$  (ego's clock);  $l$  receives it at time  $t_{2,k}$  (its clock).
- $l$  sends Delay\_Req at time  $t_{3,k}$  (its clock);  $m$  receives it at  $t_{4,k}$  (ego's clock).
- $l$  sends a second Delay\_Req\_2 at time  $t_{5,k}$  (its clock);  $m$  receives it at  $t_{6,k}$ .

After completing these message exchanges, neighbor  $l$  sends its recorded timestamps  $\{t_{2,k}, t_{3,k}, t_{5,k}\}$  to the ego  $m$ . Assuming symmetric one-way delays, a coarse estimate of clock offset and relative clock rate (or called clock skew) can be obtained as

$$\theta_k = \frac{(t_{2,k} - t_{1,k}) - (t_{4,k} - t_{3,k})}{2}, \quad (4)$$

$$\varpi_k = \frac{t_{5,k} - t_{3,k}}{t_{6,k} - t_{4,k}}. \quad (5)$$

However, a critical concern is that delays in the forward ( $m \rightarrow l$ ) and reverse ( $l \rightarrow m$ ) paths are often asymmetric. Relying on the assumption of symmetric delays can lead to significant estimation bias. To overcome this, we adopt a robust estimation scheme that models and compensates for this asymmetry, as detailed below.

2) *Clock State Model and Kalman Filtering*: Although the estimated clock offset and skew provide the clock states between vehicles, they drift over time and need to be tracked and compensated continuously. We thus model clock dynamics

as a stochastic state process and employ Kalman Filtering to estimate and correct the clock state from noisy timestamp observations.

Specifically, with the collected timestamps, we compute a time-difference measurement as

$$z_k = \tau_m^{\text{raw}}(t_k) - \tau_l^{\text{raw}}(t_k). \quad (6)$$

Here,  $\tau_m^{\text{raw}}(t_k)$  and  $\tau_l^{\text{raw}}(t_k)$  are the readings of vehicle  $m$  and  $l$ 's local clocks at  $t_k$ .  $z_k$  can be modeled as  $z_k = \mathbf{H}_k \mathbf{x} + \nu_k$  [29]. The state  $\mathbf{x} = [\theta, \varpi, b]^T$  contains the clock offset  $\theta$ , skew  $\varpi$ , and an asymmetry term  $b$  capturing forward-reverse path delay bias.  $\mathbf{H}_k = [1, \delta t_k, 1]$  maps the state to  $z_k$ , and  $\delta t_k = t_k - t_{\text{ref}}$ , where  $t_{\text{ref}}$  is a time reference.  $\nu_k$  is the measurement noise.

We discretize the clock state  $\mathbf{x}$  over interval  $\Delta t_k = t_k - t_{k-1}$ , yielding the linear update

$$\mathbf{x}_k = \Phi_k \mathbf{x}_{k-1} + \mathbf{w}_k, \quad (7)$$

$$\text{s.t. } \Phi_k = e^{F \Delta t_k} = \begin{bmatrix} 1 & \Delta t_k & 0 \\ 0 & 1 & 0 \\ 0 & 0 & 1 \end{bmatrix}, \quad F = \begin{bmatrix} 0 & 1 & 0 \\ 0 & 0 & 0 \\ 0 & 0 & 0 \end{bmatrix},$$

where  $\Phi_k$  is the state transition that advances offset by skew over  $\Delta t_k$ .  $\mathbf{w}_k$  is zero-mean Gaussian process noise with a process-noise covariance  $Q_{d,k}$ , given by

$$Q_{d,k} = \begin{bmatrix} q_\theta \Delta t_k + \frac{1}{3} q_\varpi \Delta t_k^3 & \frac{1}{2} q_\varpi \Delta t_k^2 & 0 \\ \frac{1}{2} q_\varpi \Delta t_k^2 & q_\varpi \Delta t_k & 0 \\ 0 & 0 & q_b \Delta t_k \end{bmatrix}, \quad (8)$$

where  $q_\varpi$  means the spectral density of the clock-skew random walk and  $q_b$  that of the bias drift.  $\frac{1}{3} q_\varpi \Delta t_k^3$  is the offset variance,  $\frac{1}{2} q_\varpi \Delta t_k^2$  is the offset-skew covariance,  $q_\varpi \Delta t_k$  is the skew variance, and  $q_b \Delta t_k$  is the bias-drift variance.

Since the synchronization can be formulated as a state estimation problem [30], Kalman Filtering provides an effective solution by (i) recursively integrating noisy timestamp observations, (ii) propagating estimation uncertainty (covariances) for subsequent fusion, and (iii) enabling interpolation/extrapolation under irregular measurement updates. However, in mobile environments where outliers and variable communication delays are common, the standard Gaussian-noise assumption no longer holds. To enhance robustness under such conditions, we adopt a Robust Three-Step Recursive Kalman Filter (R3SRKF) [11] scheme, as described below.

a) *Predict*: Using the state transition matrix  $\Phi_k$  and process noise  $Q_{d,k}$ , we predict the prior clock state  $\hat{x}_{k|k-1}$  and its covariance  $\mathbf{P}_{k|k-1}$ , which together provide a forecast of the expected clock difference at the  $k$ -th round:

$$\hat{x}_{k|k-1} = \Phi_k \hat{x}_{k-1|k-1}, \quad (9)$$

$$\mathbf{P}_{k|k-1} = \Phi_k \mathbf{P}_{k-1|k-1} \Phi_k^\top + Q_{d,k}, \quad (10)$$

where  $\mathbf{P}_{k|k-1} \in \mathbb{R}^{3 \times 3}$  is the predicted state covariance, its diagonals are marginal variances (e.g.,  $P_{\theta\theta}$ ), and off-diagonals are cross-covariances (e.g.,  $P_{\theta\varpi}$ ).

The prediction error and expected variance are denoted as

$$r_k = z_k - \mathbf{H}_k \hat{x}_{k|k-1}, \quad (11)$$

$$S_k = \mathbf{H}_k \mathbf{P}_{k|k-1} \mathbf{H}_k^\top + R_k. \quad (12)$$

where  $R_k > 0$  is the measurement-noise variance. We then test the normalized prediction error  $d_k^2 = r_k^2/S_k$  against a chi-squared threshold (e.g. 99% level) to detect outliers.

b) *Robust Update*: Instead of discarding large prediction errors, R3SRKF downweights them by inflating the measurement noise. We compute a weight  $\alpha_k = \min(1, \kappa/\sqrt{d_k^2})$  and set  $\tilde{R}_k = \max(R_{\min}, R_k/\alpha_k^2)$ , then update with  $\tilde{R}_k$ :

$$\tilde{S}_k = \mathbf{H}_k \mathbf{P}_{k|k-1} \mathbf{H}_k^\top + \tilde{R}_k, \quad (13)$$

$$\mathbf{K}_k = \mathbf{P}_{k|k-1} \mathbf{H}_k^\top \tilde{S}_k^{-1}, \quad (14)$$

$$\hat{x}_{k|k} = \hat{x}_{k|k-1} + \mathbf{K}_k r_k, \quad (15)$$

$$\mathbf{P}_{k|k} = (\mathbf{I} - \mathbf{K}_k \mathbf{H}_k) \mathbf{P}_{k|k-1}, \quad (16)$$

where  $\mathbf{K}_k \in \mathbb{R}^{3 \times 1}$  is the Kalman gain,  $\varepsilon$  is a stabilizer, and  $R_{\min}$  is a floor on the measurement noise. As the residual variance  $\tilde{R}_k$  increases,  $\mathbf{K}_k$  shrinks, so the state update  $\hat{x}_{k|k}$  puts less weight on low-reliability measurements, while the covariance  $\mathbf{P}_{k|k}$  stays positive semidefinite. Intuitively, when the normalized error  $d_k$  is large, the filter down-weights that observation.

After each update, the filter provides estimates  $\hat{\theta}_{k|k}$  and  $\hat{\varpi}_{k|k}$  and their covariance  $\mathbf{P}_{k|k}$ . These will be used for synchronized timestamps and uncertainty estimation, as below.

**Definition 1** (Synchronized Timestamp Mapping). *Let  $t_m$  denote the local timestamp recorded by vehicle  $m$  for a given event. This local time is mapped to the global synchronized timestamp via the following function as*

$$\text{Sync}_m(t_m) \triangleq t_m - \hat{\theta}_m - \hat{\varpi}_m(t_m - t_0), \quad (17)$$

where  $t_0 = t_{\text{ref}}$  is the reference origin. All ages below are measured on this temporal reference.

**Lemma 1** (Fusion time). *According to Definition 1, the ego vehicle's local fusion timestamp  $\hat{\tau}_f$  is mapped to the shared temporal reference, yielding the synchronized fusion instant:*

$$t_f \triangleq \text{Sync}_{\text{ego}}(\hat{\tau}_f). \quad (18)$$

**Definition 2** (Source Age at Fusion). *Let  $g_l^{\text{feat}}(t_f)$  denote the local time at which vehicle  $l$  extracted the feature used at the fusion instant  $t_f$ . Consequently, its synchronized timestamp on the common temporal reference can be expressed as:*

$$s_l(t_f) \triangleq \text{Sync}_l(g_l^{\text{feat}}(t_f)). \quad (19)$$

We define the source age of vehicle  $l$ 's feature at fusion as

$$\mathcal{S}_l(t_f) \triangleq t_f - s_l(t_f), \quad (20)$$

which captures the feature's age on the shared clock, that is, the time elapsed between its synchronized generation time  $s_l(t_f)$  and the synchronized fusion time  $t_f$ .

**Definition 3** (Arrival Age (AoI) at Fusion). *By fusion instant  $t_f$ , ego vehicle  $m$  has received multiple updates from vehicle  $l$ . Let  $g_{l \rightarrow m}^{\text{arr}}(t_f)$  denote the generation timestamp (on  $l$ 's local clock) of the most recent update that has arrived at  $m$  by  $t_f$ . Its synchronized expression is*

$$u_{l \rightarrow m}(t_f) \triangleq \text{Sync}_l(g_{l \rightarrow m}^{\text{arr}}(t_f)). \quad (21)$$

The arrival age (AoI) of the feature from  $l$  at  $m$  at the fusion instant is then defined as

$$\mathcal{A}_{l \rightarrow m}(t_f) \triangleq t_f - u_{l \rightarrow m}(t_f). \quad (22)$$

**Proposition 1.** *Given that  $u_{l \rightarrow m}(t)$  is the synchronized generation time of the most recent feature update from vehicle  $l$  received by  $m$  by time  $t$ , its evolution impacts the AoI values as follows:*

- At an arrival time  $t$ : A new feature update arrives, causing  $u_{l \rightarrow m}(t)$  to discontinuously jump to the synchronized generation time of this new update.
- Between arrivals: In the absence of new updates,  $u_{l \rightarrow m}(t)$  remains unchanged, so the AoI increases at a unit rate:  $\frac{d}{dt} \mathcal{A}_{l \rightarrow m}(t) = 1$ .

As illustrated in Fig. 3,  $\mathcal{A}_{l \rightarrow m}(t)$  follows a sawtooth evolution: it resets to the current end-to-end delay at each feature arrival and increases with unit slope in between.

While Definition 3 specifies the arrival AoI  $\mathcal{A}_{l \rightarrow m}(t_f)$ , it characterizes only the features already received by the fusion time. It does not account for features that have not yet been transmitted, for which a predictive AoI measure is required to guide transmission decisions. To this end, we introduce a delivery-time AoI, which predicts the age a Region of Interest (RoI) will have when it arrives at the receiver.

**Definition 4** (Delivery-Time AoI). *Given fusion instant  $t_f$  and RoI  $r$  from vehicle  $l$ , let  $\widehat{\Delta t}_{\text{comm}}(l \rightarrow m, r, t_f)$  denote the communication delay from  $l$  to  $m$  for  $r$ . We define the delivery-time AoI as*

$$\tilde{\mathcal{A}}_{l \rightarrow m}(r, t_f) \triangleq \mathcal{S}_l(t_f) + \widehat{\Delta t}_{\text{comm}}(l \rightarrow m, r, t_f). \quad (23)$$

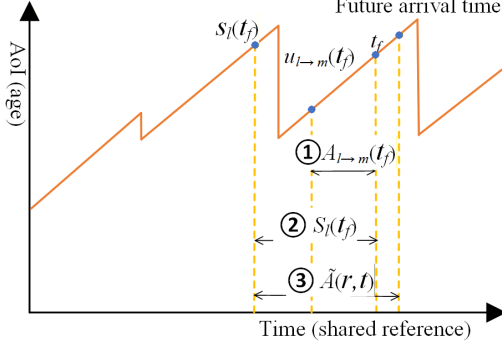


Fig. 3: AoI and related metrics on a shared time reference:  $s_l(t_f)$  (feature generation time),  $u_{l \rightarrow m}(t_f)$  (latest arrived generation time),  $t_f$  (fusion time), and  $t_f + \Delta t_{\text{comm}}(l \rightarrow m, r, t_f)$  (predicted arrival time). Brackets: ①  $\mathcal{A}_{l \rightarrow m}(t_f)$ , ②  $S_l(t_f)$ , ③  $\tilde{\mathcal{A}}_{l \rightarrow m}(r, t_f)$ .

This estimates how old  $r$  will be upon its availability at the receiver. The calculation of  $\tilde{\Delta t}_{\text{comm}}$  will be detailed in the subsequent section.

We next present an example case study to illustrate these definitions.

**Example 1.** Let the reference origin be  $t_0 = 0$ . Suppose the ego vehicle and vehicle  $l$  have the estimated clock parameters:  $\hat{\theta}_{\text{ego}} = 0.12$  s,  $\hat{\omega}_{\text{ego}} = 0.002$ ,  $\hat{\theta}_l = -0.06$  s,  $\hat{\omega}_l = -0.001$ .

(1) **Fusion time  $t_f$ :** The ego records a local fusion timestamp  $\hat{t}_f = 10.25$  s. By Definition 1,

$$\begin{aligned} t_f &= \text{Sync}_{\text{ego}}(\hat{t}_f) = 10.25 - 0.12 - 0.002(10.25 - 0) \\ &= 10.1095 \text{ s}. \end{aligned}$$

(2) **Source age at fusion  $S_l(t_f)$ :** Assume the feature from vehicle  $l$  used at fusion was extracted at local time  $g_l^{\text{feat}}(t_f) = 9.18$  s. Its synchronized expression is

$$\begin{aligned} s_l(t_f) &= \text{Sync}_l(g_l^{\text{feat}}(t_f)) = 9.18 - (-0.06) - (-0.001)9.18 \\ &= 9.24918 \text{ s}. \end{aligned}$$

Hence the source age is

$$S_l(t_f) = t_f - s_l(t_f) = 10.1095 - 9.24918 \approx 0.86 \text{ s}.$$

(3) **Arrival AoI  $\mathcal{A}_{l \rightarrow m}(t_f)$ :** By  $t_f$ , let the newest update from  $l$  that has arrived at  $m$  have local generation time  $g_{l \rightarrow m}^{\text{arr}}(t_f) = 9.55$  s. Its synchronized expression is

$$\begin{aligned} u_{l \rightarrow m}(t_f) &= \text{Sync}_l(g_{l \rightarrow m}^{\text{arr}}(t_f)) \\ &= 9.55 - (-0.06) - (-0.001)9.5 = 9.61955 \text{ s}, \\ \text{so } \mathcal{A}_{l \rightarrow m}(t_f) &= t_f - u_{l \rightarrow m}(t_f) \\ &= 10.1095 - 9.61955 = 0.48995 \text{ s} \approx 0.49 \text{ s}. \end{aligned}$$

(4) **Delivery-Time AoI  $\tilde{\mathcal{A}}_{l \rightarrow m}(r, t_f)$ :** For a not-yet-available region  $r$ , suppose the predicted delay is  $\hat{\Delta t}_{\text{comm}} = 0.40$  s. Then the projected AoI upon arrival is

$$\begin{aligned} \tilde{\mathcal{A}}_{l \rightarrow m}(r, t_f) &= S_l(t_f) + \hat{\Delta t}_{\text{comm}} \\ &= 0.86032 + 0.40 = 1.26032 \text{ s} \approx 1.26 \text{ s}. \end{aligned}$$

3) **Temporal Uncertainty Analysis:** Once Kalman Filtering provides the state estimate and their associated covariance, we can quantify not only the current synchronization quality but also its expected degradation over time without further updates. This predictive capability is essential for downstream decision-making, as it reveals how quickly temporal uncertainty accumulates and when it becomes detrimental to the downstream fusion.

We therefore decompose how temporal uncertainty grows if no new timestamp message arrives for a duration  $\Delta t$ :

$$\sigma_\theta^2(\Delta t) = P_{\theta\theta} + 2\Delta t P_{\theta\varpi} + \Delta t^2 P_{\varpi\varpi} + q_\theta \Delta t + \frac{1}{3} q_\varpi \Delta t^3. \quad (24)$$

These terms show how temporal uncertainty can grow rapidly with  $\Delta t$ , especially the skew-related terms. From left to right are: current offset variance; linear drift term (coupling between offset and skew); variance from clock skew growing over time; linear growth from phase noise; and cubic term from integrated skew noise.

Note that the synchronized timestamp mapping  $\text{Sync}(\cdot)$  from Definition 1 removes relative bias, while  $P_{\theta\theta}$  quantifies the temporal uncertainty propagated to the downstream.

4) **Propagation of Temporal to Spatial Misalignment:** A residual temporal uncertainty inevitably manifests as a spatial feature misalignment for moving objects. Let  $\delta t_{l \rightarrow m}$  denote the temporal reference between the ego  $m$  and neighbor  $l$ , and let  $\mathbf{v}(r)$  be the RoI's relative velocity to the ego  $m$ 's coordinate system. Then the induced spatial displacement is

$$\Delta \mathbf{p}_{\text{time} \rightarrow \text{space}}(r) \approx \mathbf{v}(r) \delta t_{l \rightarrow m}. \quad (25)$$

If  $\delta t_{l \rightarrow m}$  is zero-mean with variance  $\sigma_t^2$ , the expected squared displacement satisfies

$$\sigma_{\text{time} \rightarrow \text{space}}^2(r) \approx \mathbb{E}[\|\Delta \mathbf{p}(r)\|^2] = \|\mathbf{v}(r)\|^2 \sigma_t^2. \quad (26)$$

Eq. (26) validates that faster-moving objects incur greater spatial feature misalignment for a given temporal uncertainty. We will combine this with purely spatial uncertainty in Section III-D4 to form a total uncertainty metric.

### C. Communication Model

Even with perfectly synchronized clocks, communication delay will affect how fresh the received data is. We next model communication conditions for sharing information.

1) **Channel Conditions:** Assuming an Orthogonal Frequency Division Multiple Access (OFDMA) wireless network, let  $\mathcal{E} = \{1, 2, \dots, E\}$  denote the set of orthogonal subchannels. If each vehicle uses at most one subchannel, up to  $E$  vehicles can transmit simultaneously. Let  $\ell \in (L \cup \{\text{RSU}\})$  index a receiver (neighbor vehicle or RSU). The signal-to-interference-plus-noise ratio (SINR) from ego  $m$  to  $\ell$  is [6]

$$\gamma_{m,\ell}(e) = \frac{P_m(e) h_{m,\ell}(e)}{\sum_{i \in \mathcal{I}_e} P_i(e) h_{i,\ell}(e) + N_0 \beta_e}, \quad (27)$$

where  $P_m(e)$  is  $m$ 's transmit power on subchannel  $e$ ,  $h_{m,\ell}(e)$  is the channel gain,  $\mathcal{I}_e$  is the set of co-channel interferers on subchannel  $e$ ,  $N_0$  is the noise spectral density,  $\beta_e$  is the

bandwidth of subchannel  $e$ . Under ideal OFDMA orthogonality within the coverage area, we set  $\mathcal{I}_e = \emptyset$  and  $\eta_e \approx 0$ , in which case (27) reduces to an SNR.

Therefore, the uplink data rate from  $l$  to  $m$  is

$$\mu_{l,m} = \sum_{e \in E} \beta_e \log_2 (1 + \gamma_{l,m}^e) (1 - \Lambda_{l,m}^e), \quad (28)$$

where  $\Lambda_{l,m}^e$  is the packet error rate (PER) on sub-channel  $e$ , obtained from the modulation and coding scheme (MCS) mapping [31]. For example, with uncoded Quadrature Phase Shift Keying (QPSK) and packet length  $L_{\text{pkt}}$ ,  $\Lambda_{l,m}^e \approx 1 - (1 - Q(\sqrt{2\gamma}))^{L_{\text{pkt}}}$ . In practice, we can use a lookup table for SINR-to-PER [32].

Using the above rate, we next consider how much time it takes to send an ROI.

2) *Transmission Cost*: In IoV systems, communication efficiency can be improved by transmitting only ROIs rather than the entire feature map. Each ROI is quantized with  $q$  (measured in bits per feature channel), where a higher  $q$  retains more feature detail at the cost of increased bitrate. Formally, the bit cost of transmitting an ROI  $r$  is given by:

$$\mathcal{B}(q, r) = q \cdot C_{\text{feat}} \cdot \mathcal{E}(r), \quad (29)$$

where  $\mathcal{C}_\theta(\cdot)$  operates per BEV grid and models the temporal evolution along the  $\mathcal{K}$  observations.

Based on the above models, the estimated transmission delay can be calculated as

$$\hat{\Delta}t_{\text{comm}}(l \rightarrow m, r, t_f) = \frac{\mathcal{B}(q, r)}{\mu_{l,m}(t_f)}. \quad (30)$$

Therefore, Definition 4 can be derived, to decide whether to send a region and at what quality so that it can realize the timely feature exchange.

#### D. Spatiotemporal Feature Alignment

To achieve spatiotemporal feature alignment, we perform a geometric projection of neighbor features into the ego vehicle's coordinate frame, and then design a temporal compensator to correct the discrepancies induced by their asynchronous generation times.

1) *Geometric Projection*: We define  $\mathcal{F}_l(t)$  as the body-fixed frame of vehicle  $l$  at shared time  $t$ . This frame is determined by the vehicle's estimated pose (position and orientation) and serves as the local reference for expressing data points or feature maps captured at that instant. It is crucial to distinguish *coordinate frames* from *feature maps* in our context:  $\mathcal{F}$  denotes a geometric reference frame, while  $\mathcal{F}_l(t)$  is the feature vector produced by vehicle  $l$  at time  $t$  and defined over a frame anchored in  $\mathcal{F}$ . Given this, the transformation  $\mathcal{T}_{m(t_1) \rightarrow l(t_2)}$  maps a point  $\mathbf{X}$  from  $\mathcal{F}_m(t_1)$  to  $\mathcal{F}_l(t_2)$ :

$$\mathcal{T}_{m(t_1) \rightarrow l(t_2)} \mathbf{X} = R_{m \rightarrow l}(t_1, t_2) \mathbf{X} + N_{m \rightarrow l}(t_1, t_2), \quad (31)$$

where the relative rotation  $R_{m \rightarrow l}$  and translation  $N_{m \rightarrow l}$  are obtained from the estimated poses of  $m$  at  $t_1$  and  $l$  at  $t_2$ .

Given the fusion time  $t_f$ , we define the ego's frame  $\mathcal{F}_m(t_f)$  as the common supervision frame. To this end, we sample

the ego's feature map into the fusion-aligned frame of each neighbor  $l$ :

$$\mathbf{F}_m^{\text{sup} \rightarrow l}(t_f) = \mathcal{W}(\mathbf{F}_m^{\text{sup}}(t_f); \mathcal{T}_{m(t_f) \rightarrow l(t_f)}), \quad (32)$$

where  $\mathcal{W}(\cdot; \mathcal{T})$  denotes warping a feature map by the transformation  $\mathcal{T}$  [33].

We begin by synchronizing the generation time of each historical feature. For the  $\kappa$ -th feature from vehicle  $l$ , its synchronized time is  $s_l^{(\kappa)}$ . Subsequently, we perform an intra-vehicle geometry projection to align all of  $l$ 's features to a common temporal reference, transforming each feature from  $\mathcal{F}_l(s_l^{(\kappa)})$  to  $\mathcal{F}_l(t_f)$ :

$$\mathbf{F}_l^{(t_\kappa \rightarrow t_f)} = \mathcal{W}(\mathbf{F}_l(t_\kappa); \mathcal{T}_{l(s_l^{(\kappa)}) \rightarrow l(t_f)}). \quad (33)$$

As the final fusion occurs at the ego frame  $\mathcal{F}_m(t_f)$ , we perform an inter-vehicle projection:

$$\tilde{\mathbf{F}}_l^{(t_\kappa \rightarrow t_f)} = \mathcal{W}(\mathbf{F}_l^{(t_\kappa \rightarrow t_f)}; \mathcal{T}_{l(t_f) \rightarrow m(t_f)}). \quad (34)$$

While the geometric transformations align the *spatial reference* of all features by compensating for vehicle motion and projecting them into  $\mathcal{F}_m(t_f)$ , they leave the *temporal content* unchanged. Each aligned feature map  $\tilde{\mathbf{F}}_l^{(t_\kappa \rightarrow t_f)}$  still depicts the scene at its original observation time  $s_l^{(\kappa)}$ . To correct the misalignment arising from dynamic object motion between  $s_l^{(\kappa)}$  and  $t_f$ , a *temporal compensation* step is required.

2) *Temporal Compensation*: Given the spatially aligned feature stack  $\{\tilde{\mathbf{F}}_l^{(t_\kappa \rightarrow t_f)}\}_{\kappa=1}^{\mathcal{K}}$ , we proceed to correct their temporal staleness. To this end, we utilize the source ages of the features. According to Definition 2, the  $\kappa$ -th feature, has a source age  $\mathcal{S}_l^{(\kappa)}(t_f)$ . We collect these ages into a vector  $\mathbf{a}_l(t_f) = (\mathcal{S}_l^{(1)}(t_f), \dots, \mathcal{S}_l^{(\mathcal{K})}(t_f))$ .

A temporal compensator  $\mathcal{C}_\theta(\cdot)$  predicts the feature at  $t_f$  from the spatially aligned stack and their source ages:

$$\hat{\mathbf{F}}_l(t_f) = \mathcal{C}_\theta\left(\{\tilde{\mathbf{F}}_l^{(t_\kappa \rightarrow t_f)}\}_{\kappa=1}^{\mathcal{K}}, \mathbf{a}_l(t_f)\right), \quad (35)$$

where  $\mathcal{C}_\theta(\cdot)$  operates per BEV grid and models the temporal evolution along the  $\mathcal{K}$  observations. For each spatial grid, we form a short feature sequence over time and augment it with the corresponding AoI values  $\mathcal{S}_l^{(\kappa)}(t_f)$  as continuous temporal conditions. A lightweight Conv1D block is adopted as the temporal compensator to propagate these features from their original timestamp  $s_l^{(\kappa)}$  to  $t_f$  in the frame  $\mathcal{F}_m(t_f)$ , producing an aligned feature  $\hat{\mathbf{F}}_l(t_f)$  in frame  $\mathcal{F}_m(t_f)$ . Such temporal 1-D convolutions have been shown to effectively capture local sequential dependencies while remaining efficient and stable for short-term temporal modeling, outperforming recurrent models in parallelism and convergence stability [34].

Overall, our scheme enables geometric projection to align *where* features are expressed and temporal compensation to align *when* they represent. This decoupling simplifies learning, as  $\mathcal{C}_\theta$  only needs to model temporal evolution within a fixed coordinate frame.

3) *Alignment Objective*: For supervision, we use the ego's feature map at the fusion instant,  $\mathbf{F}_m^{\text{sup}}(t_f)$ , as the target in the ego frame  $\mathcal{F}_m(t_f)$ . To enable temporal alignment, we train the model by matching the neighbor's temporally compensated feature  $\hat{\mathbf{F}}_l(t_f)$ , which is already expressed in the ego frame, against this target using a Smooth- $L_1$  loss:

$$\mathcal{L}_{\text{align}} = \text{SmoothL}_1(\hat{\mathbf{F}}_l(t_f), \mathbf{F}_m^{\text{sup}}(t_f)). \quad (36)$$

At inference, ground truth targets are unavailable, so we propagate time-induced and spatial uncertainties to form a reliability score, which is then used for weighted fusion.

4) *Uncertainty-Derived Reliability*: As stated, spatiotemporal feature misalignment is inevitable in collaborative perception. Two features with identical AoI may exhibit different synchronization and alignment errors. This motivates us to quantify uncertainties in the synchronization and alignment processes, especially under dynamic heterogeneous conditions [35], [36].

Given an ROI  $r$  from vehicle  $l$ , let  $p_l^{(\kappa)}(r)$  denote the center of this ROI in  $l$ 's local coordinate frame. This center can be geometrically transformed into the ego vehicle's fusion frame, where the corresponding reference center is denoted as  $p_m(r)$ , so we have:

$$\hat{p}_m^{(\kappa)}(r) = \mathcal{T}_{l(s_l^{(\kappa)}) \rightarrow m(t_f)} p_l^{(\kappa)}(r), \quad (37)$$

$$\delta_{ml}^{(\kappa)}(r) = \hat{p}_m^{(\kappa)}(r) - p_m(r). \quad (38)$$

Over  $\Gamma$  samples (drawn across  $\mathcal{K}$  frames and  $L$  neighbors), we can estimate the covariance [37]:

$$\hat{\Sigma}_{\text{space}}(r) = \frac{1}{\Gamma-1} \sum_{i=1}^{\Gamma} (\delta_{ml}^{(i)}(r) - \bar{\delta}(r)) (\delta_{ml}^{(i)}(r) - \bar{\delta}(r))^{\top}, \quad (39)$$

with  $\bar{\delta}(r) = \frac{1}{\Gamma} \sum_{i=1}^{\Gamma} \delta_{ml}^{(i)}(r)$ . Then the spatial variance is

$$\sigma_{\text{space}}^2(r) = \text{tr}(\hat{\Sigma}_{\text{space}}(r)). \quad (40)$$

Hence, ROI  $r$ 's total uncertainty is the sum of spatial variance and the time-induced terms:

$$\begin{aligned} \sigma_{l \rightarrow m}^2(r) &= \sigma_{\text{space}}^2(r) + \sigma_{\text{time} \rightarrow \text{space}}^2(r) \\ &= \sigma_{\text{space}}^2(r) + \|\mathbf{v}(r)\|^2 \sigma_t^2. \end{aligned} \quad (41)$$

We convert this uncertainty into a reliability metric for downstream fusion:

$$c_{l \rightarrow m}(r) = \exp\left(-\frac{\sigma_{l \rightarrow m}^2(r)}{\tau_c^2}\right), \quad (42)$$

with scale parameter  $\tau_c$ . As expected, high motion under poor synchronization or inaccurate alignment leads to a larger  $\sigma_{l \rightarrow m}^2(r)$  and thus a smaller  $c_{l \rightarrow m}(r)$ .

### E. Weighted Feature Fusion

After spatiotemporal feature alignment, for efficient fusion, we need to determine how much each aligned feature contributes to the fusion.

According to Definitions 3-4, we have two types of AoIs. Although the arrival AoI  $\mathcal{A}_{l \rightarrow m}(t_f)$  quantifies the staleness of

features that have already arrived, it is typically unavailable at decision time. Consequently, adopting delivery-time AoI  $\tilde{\mathcal{A}}_{l \rightarrow m}(r, t_f)$  is more tractable in our framework.

Given the reliability  $c_{l \rightarrow m}(r)$ , the normalized ROI weight can be obtained as

$$\alpha_{l \rightarrow m}(r) = \frac{c_{l \rightarrow m}(r) \exp(-\tilde{\mathcal{A}}_{l \rightarrow m}(r))}{\sum_{l'} c_{l' \rightarrow m}(r) \exp(-\tilde{\mathcal{A}}_{l' \rightarrow m}(r))}. \quad (43)$$

With a  $1 \times 1$  projection  $\mathbf{W}_{\text{fuse}}$  that aligns feature channels across vehicles, their fused feature at time  $t_f$  is given by

$$\mathbf{F}_{\text{out}}(t_f) = \mathbf{F}_m(t_f) + \sum_l \alpha_{l \rightarrow m} \odot (\mathbf{W}_{\text{fuse}} \hat{\mathbf{F}}_l(t_f)), \quad (44)$$

where  $\odot$  denotes elementwise scaling.  $\alpha_{l \rightarrow m}$  encodes freshness and reliability, and is applied per-ROI, so each ROI's contribution is modulated by both.

We supervise fusion with an  $L_2$  loss between the fused feature and the ground-truth at  $t_f$ :

$$\mathcal{L}_{\text{fuse}} = \|\mathbf{F}_{\text{out}}(t_f) - \mathbf{F}_m^{\text{sup}}(t_f)\|_2^2. \quad (45)$$

For implementation, we will train the overall perception model by minimizing the total loss, which includes both the alignment and fusion losses, i.e.,  $\min(\mathcal{L}_{\text{align}} + \mathcal{L}_{\text{fuse}})$ .

## IV. EVALUATIONS

In this section, we simulate the proposed framework and compare it against representative baselines for collaborative perception in IoV scenarios.

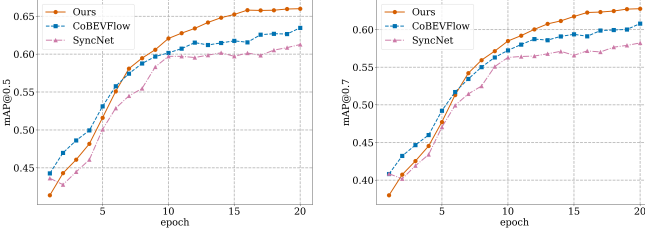
### A. Simulation Setup

We evaluate on a LiDAR-based 3D object detection task using V2X-Sim [38], [39], generated via SUMO [40] and CARLA [41]. This dataset provides high-resolution 3D point clouds and bounding box annotations. These raw point clouds are first cropped and voxelized before being projected onto a BEV map with dimensions  $256 \times 256 \times 13$ .

1) *Data Generation and Processing*: Each scene contains up to 6 agents (vehicles and an RSU). Agent 1 is treated as the center (ego) agent. For each scene and each agent, we perform the following setups to generate metadata beyond traditional visual features.

a) *Network Synchronization*: To emulate unsynchronized clocks, each agent  $\ell$  is assigned a stochastic local clock:  $\tau_{\ell}^{\text{raw}}(t) = \theta_{\ell} + \varpi_{\ell} t + \varepsilon_{\ell}(t)$ , where the initial offset  $\theta_{\ell}$  follows  $\mathcal{U}(-10, 10)$  ms, skew  $\varpi_{\ell}$  follows  $\mathcal{N}(0, 5 \text{ ppm})$ , and jitter  $\varepsilon_{\ell}(t)$  is modeled as a discrete-time AR(1) process, namely Auto-Regressive process of order 1, with coefficient  $\phi = 0.7$  and standard deviation 0.2 ms. For each scene, we simulate a PTP-based two-way timestamp exchange and apply Kalman filtering to obtain synchronized clock estimates as defined.

b) *Communication Condition*: The communication condition is drawn with bandwidth  $\beta = 1.8$  MHz and SNR is  $\gamma = 10^{\gamma_{\text{dB}}/10}$  with  $\gamma_{\text{dB}} \sim \mathcal{N}(10, 2^2)$ , yielding spectral efficiency  $\eta = \log_2(1 + \gamma)$ . PER is modeled as a logistic in  $\gamma_{\text{dB}}$ ,  $\Lambda = \left(1 + \exp(\zeta(\gamma_{\text{dB}} - \gamma_0))\right)^{-1}$  with  $\zeta = 1$ ,  $\gamma_0 = 6$  dB. Therefore, effective data rate is  $\mu = \beta \eta (1 - \Lambda)$  bps. Moreover,



(a) mAP@0.5.

(b) mAP@0.7.

Fig. 4: Performance comparison of various schemes, including our proposed method, CoBEVFlow, and SyncNet, evaluating their (a) mAP@0.5, and (b) mAP@0.7.

the bit budget to transmit an ROI  $r$  is approximated by  $\mathcal{B}(q, r) \approx N_g(r) C_{\text{feat}} q$  bits, where  $N_g(r) = \left\lceil \frac{w(r)}{\Delta_x} \cdot \frac{l(r)}{\Delta_y} \right\rceil$  is the ROI's grid footprint, computed from its width  $w(r)$  and length  $l(r)$  at the BEV grid resolutions  $(\Delta_x, \Delta_y)$ , and the value of  $q$  is set as 16.

All simulations are implemented in PyTorch and run on an NVIDIA RTX A6000 GPU. Training uses Adam optimizer with learning rate  $10^{-3}$  and batch size 1.

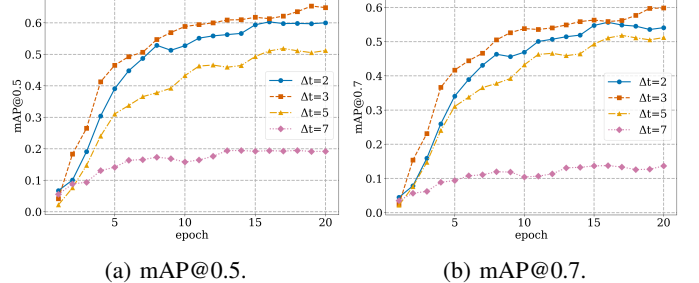
#### B. Performance Comparison of Different Collaborative Perception Algorithms

We compare the performance of our proposed spatiotemporal feature alignment and weighted fusion algorithm with other baselines, as described below.

- **The proposed method** establishes a shared temporal reference via network synchronization, computes AoI on this basis, and performs spatiotemporal feature alignment using these AoIs. The fusion weights for each ROI jointly consider AoI and uncertainty-derived reliability, prioritizing fresh and certain features.
- **CoBEVFlow** [18] compensates for asynchrony by learning a BEV flow field to spatially warp sender features from their original timestamps to the receiver's time, treating the provided timestamps as accurate. The warped features are then fused and decoded.
- **SyncNet** [17] addresses latency by using a temporal prediction network to extrapolate the current feature map from a sequence of past observations. The predicted feature is subsequently fused and decoded for perception.

For evaluation, we compute Average Precision (AP) for the center agent at IoU thresholds of 0.5 and 0.7 using the standard evaluation over class-conditioned precision-recall curves.

As shown in Fig. 4, our method achieves higher perception accuracy than CoBEVFlow and SyncNet across both IoU thresholds. While CoBEVFlow exhibits a marginally faster initial rise, our approach surpasses it around epochs 6-8 and continues to widen the performance gap throughout the middle to late training stages. Such advantages of our method stem from its ability to mitigate temporal drift before fusion. Furthermore, the reliability weighting suppresses regions with residual misalignment, preventing poorly aligned features from degrading fusion quality. Together, these components not



(a) mAP@0.5.

(b) mAP@0.7.

Fig. 5: Impact of temporal misalignment, from 2 to 7 timestamps, evaluating their (a) mAP@0.5, and (b) mAP@0.7.

only enhance accuracy but also improve training efficiency, enabling faster convergence and better final performance with less computation overhead.

#### C. Impact of Temporal Misalignment

Subsequently, we evaluate the impact of temporal misalignment. To emulate unsynchronized operation, we adopt a hybrid temporal process in which each scene is initialized with a major time offset of  $\Delta t \in \{2, 3, 5, 7\}$ , followed by additional inter-agent time gaps introduced through clock-drift and network-delay modeling.

As shown in Fig. 5, when the misalignment level is small ( $\Delta t \leq 3$ ), the model converges rapidly and sustains stable improvements, indicating that our proposed method can handle a mild level of time misalignment for accurate feature fusion. Notably,  $\Delta t = 3$  slightly outperforms  $\Delta t = 2$  in later epochs, suggesting that modest temporal diversity can regularize learning and improve robustness. As the misalignment grows to  $\Delta t = 5$ , performance degrades and saturates at a lower plateau, suggesting that the temporal discrepancy exceeds the backbone's tolerance, limiting the benefit of collaboration. At  $\Delta t = 7$ , perception accuracy remains below 0.2 for mAP@0.5 and 0.15 for mAP@0.7, meaning that excessive misalignment injects stale information inevitably, which our scheme cannot effectively compensate for.

To complement the quantitative results, Fig. 6 visualizes the impact on spatial feature consistency. For  $\Delta t \in \{2, 3\}$ , predicted boxes remain well aligned with ground truth, covering most vehicles with correct positions and orientations. At  $\Delta t = 5$ , subtle degradation appears, boxes shift or partially mismatch, especially for distant or occluded targets, mirroring the drop in mAP curves (Fig. 5). At  $\Delta t = 7$ , degradation becomes severe, and missed detections and false positives at outdated positions indicate that fused features hardly describe a consistent scene.

Overall, these results reveal an offset tolerance of approximately  $\Delta t \approx 3$ . Within this range, our proposed method can enhance cooperative perception by leveraging complementary viewpoints across vehicles; beyond it, temporal misalignment cannot be effectively mitigated, hindering the collaboration perception results.

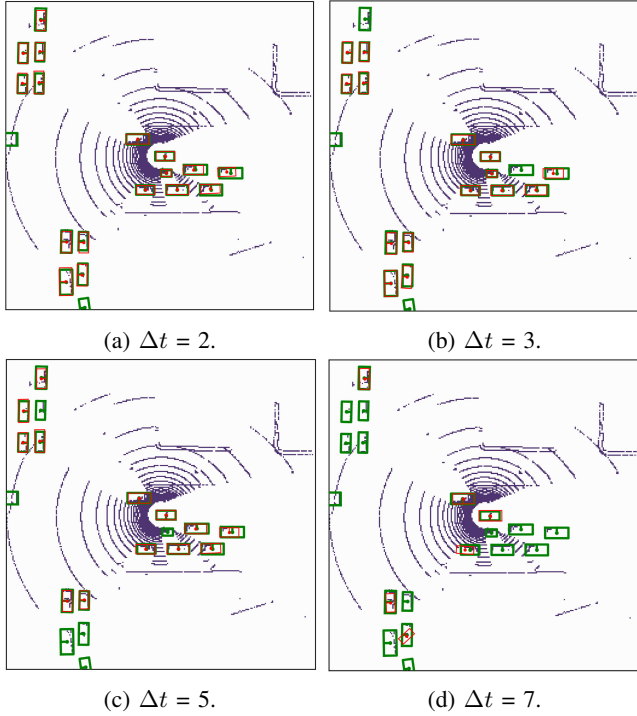


Fig. 6: Visualization of time misalignment impact, from 2 to 7 timestamps. Green boxes represent the ground truth, and red boxes are the detected ones.

#### D. Ablation Study

To quantify the contribution of each component, we conduct ablations that selectively disable synchronization and communication-delay modeling, including:

- **Full model** employs full network synchronization to establish a shared clock, computes AoI on this reference, models communication delays, performs spatiotemporal feature alignment, and applies joint AoI-reliability weighting during ROI-level fusion.
- **No clock** scheme disables network synchronization and AoI computation. Each agent operates on its local timestamps, while communication-delay modeling and the downstream fusion pipeline are retained.
- **No communication delay** variant maintains network synchronization and AoI computation but removes link-delay modeling by assuming instantaneous feature delivery. All other processing components remain active.

From Fig. 7, we can see that removing either synchronization or communication delay leads to a consistent drop in performance across both IoU thresholds. *No clock* variant suffers the most, its curve rises slowly in the early epochs and levels off well below the full model. At mAP@0.7, the final accuracy is about 7-8 points lower, while at mAP@0.5 the gap remains around 6-7 points. This degradation is expected because, without a shared clock, features from different vehicles arrive with uncontrolled drift, and the fusion process cannot properly align them even after spatial domain transformations. *No communication delay* variant shows intermediate behavior. Its curves initially track our method more closely, but once

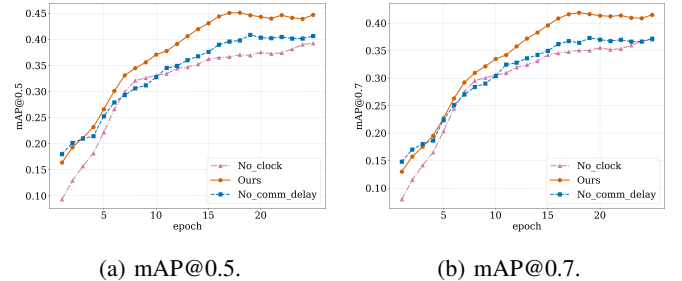


Fig. 7: Performance comparison of ablation schemes, including our proposed method, and schemes without network synchronization or communication delay modeling, evaluating their (a) mAP@0.5, and (b) mAP@0.7.

training stabilizes the gap becomes clear. These results indicate that unmodeled communication delays leave subtle but persistent feature staleness, leading to degraded fusion performance.

## V. CONCLUSION

Collaborative perception promises broader scene coverage and improved decision-makings in IoV systems by aggregating vehicle observations, but their fusion quality and efficiency are often degraded, due to unsynchronized clocks, fluctuating delays, and inefficient feature sharing. To address these challenges, we have proposed a spatiotemporal feature alignment and weighted fusion framework by network synchronization and AoI. First, we have maintained a shared temporal reference, by estimating inter-vehicle clock state and mapping all timestamps onto it. On this reference, AoI has been calculated, which considers time since generation with an estimated communication delay, so it reflects the predicted features' state at fusion. Guided by this, alignment has been proceeded spatiotemporally, where geometric warping brings all features into one spatial coordinate frame, and an AoI-conditioned temporal compensator reconciles time gaps to the common fusion instant. We have further integrated time-to-space and spatial uncertainties into a reliability metric, and combined with AoI to perform ROI-level weighted fusion for improving efficiency. Simulations with clock drift and communication delay have also shown consistent gains over strong baselines. Ablations have confirmed that synchronization and communication modeling both contribute to the overall improvement.

In the future, we will build a task-aware, end-to-end collaborative perception system. This pursuit will unfold in two key thrusts: first, by creating a perception-communication co-design that dynamically optimizes data sharing under resource constraints; and second, by building a unified multimodal model that fuses LiDAR, cameras, and radar, and couples perception with planning to form a closed-loop system where decision needs guide sensing and fusion actions.

## REFERENCES

[1] N. Shakya, F. Li, and J. Chen, “On distributed computing with heterogeneous communication constraints,” *IEEE/ACM Trans. Netw.*, vol. 30, no. 6, pp. 2776–2787, 2022.

[2] B. McMahan, E. Moore, D. Ramage, S. Hampson, and B. A. y Arcas, "Communication-efficient learning of deep networks from decentralized data," in *Proc. 20th Int. Conf. Artificial Intelligence and Statistics*, 2017, pp. 1273–1282.

[3] D.-J. Han, H. I. Bhatti, J. Lee, and J. Moon, "Accelerating federated learning with split learning on locally generated losses," in *Proc. FL-ICML*, 2021.

[4] H. Han, H. Liu, C. Yang, and J. Qiao, "Transfer learning algorithm with knowledge division level," *IEEE Trans. Neural Netw. Learn. Syst.*, pp. 1–15, 2022.

[5] J. Shu, W. Zhang, Y. Zhou, Z. Cheng, and L. T. Yang, "Flas: Computation and communication efficient federated learning via adaptive sampling," *IEEE Trans. Netw. Sci. Eng.*, vol. 9, no. 4, pp. 2003–2014, 2022.

[6] Q. Han, X. Wang, and W. Shen, "Communication-dependent computing resource management for concurrent task orchestration in IoT systems," *IEEE Trans. Mob. Comput.*, vol. 23, no. 12, pp. 14 297–14 312, 2024.

[7] M. K. Abdel-Aziz, C. Perfecto, S. Samarakoon, M. Bennis, and W. Saad, "Vehicular cooperative perception through action branching and federated reinforcement learning," *IEEE Trans. Commun.*, vol. 70, no. 2, pp. 891–903, 2022.

[8] Q. Xie, X. Zhou, T. Hong, W. Hu, W. Qu, and T. Qiu, "Towards communication-efficient cooperative perception via planning-oriented feature sharing," *IEEE Trans. Mobile Comput.*, pp. 1–14, 2024.

[9] M. Usman, M. Qaraqe, M. R. Asghar, A. A. Gebremariam, I. S. Ansari, F. Granelli, and Q. H. Abbasi, "A business and legislative perspective of V2X and mobility applications in 5G networks," *IEEE Access*, vol. 8, pp. 67 426–67 435, 2020.

[10] P. Jia, X. Wang, and X. Shen, "Accurate and efficient digital twin construction using concurrent end-to-end synchronization and multi-attribute data resampling," *IEEE Internet Things J.*, vol. 10, no. 6, pp. 4857–4870, 2023.

[11] X. Liu and H. Wang, "Robust clock parameters tracking for IEEE 1588 with asymmetric packet delays in industrial networks," *IEEE Trans. Commun.*, vol. 73, no. 2, pp. 1248–1261, 2025.

[12] E. Arnold, M. Dianati, R. de Temple, and S. Fallah, "Cooperative perception for 3D object detection in driving scenarios using infrastructure sensors," *IEEE Trans. Intell. Transp. Syst.*, vol. 23, no. 3, pp. 1852–1864, 2022.

[13] L. Chen, Y. Li, C. Huang, B. Li, Y. Xing, D. Tian, L. Li, Z. Hu, X. Na, Z. Li, S. Teng, C. Lv, J. Wang, D. Cao, N. Zheng, and F.-Y. Wang, "Milestones in autonomous driving and intelligent vehicles: Survey of surveys," *IEEE Trans. Intell. Veh.*, vol. 8, no. 2, pp. 1046–1056, 2023.

[14] Q. Han, X. Wang, and W. Shen, "Distributed link heterogeneity exploitation for attention-weighted robust federated learning in 6G networks," in *Proc. IEEE Conf. Comput. Commun. Workshops*, 2024, pp. 1–6.

[15] Q. Chen, S. Tang, Q. Yang, and S. Fu, "Cooper: Cooperative perception for connected autonomous vehicles based on 3D point clouds," in *Proc. Int. Conf. Distrib. Comput. Syst.*, 2019, pp. 514–524.

[16] R. Xu, H. Xiang, Z. Tu, X. Xia, M.-H. Yang, and J. Ma, "V2x-VIT: Vehicle-To-Everything Cooperative Perception with Vision Transformer," in *Proc. Eur. Conf. Comput. Vis.* Springer, 2022, pp. 107–124.

[17] Z. Lei, S. Ren, Y. Hu, W. Zhang, and S. Chen, "Latency-aware collaborative perception," in *Proc. Eur. Conf. Comput. Vis.*, 2022, pp. 316–332.

[18] S. Wei, Y. Wei, Y. Hu, Y. Lu, Y. Zhong, S. Chen, and Y. Zhang, "Asynchrony-robust collaborative perception via bird's eye view flow," *Proc. Int. Conf. Adv. Neural Inf. Process. Syst.*, vol. 36, pp. 28 462–28 477, 2023.

[19] Y.-C. Liu, J. Tian, C.-Y. Ma, N. Glaser, C.-W. Kuo, and Z. Kira, "Who2com: Collaborative perception via learnable handshake communication," in *Proc. IEEE Int. Conf. Robot. Automat.* IEEE, 2020, pp. 6876–6883.

[20] Y. Hu, S. Fang, Z. Lei, Y. Zhong, and S. Chen, "Where2comm: Communication-Efficient Collaborative Perception via Spatial Confidence Maps," *Proc. Adv. Neural Inf. Process. Syst.*, vol. 35, pp. 4874–4886, 2022.

[21] M. Bezmenov, M. Frey, Z. Utkovski, and S. Stanczak, "An age of information characterization of SPS for V2X applications," *arXiv preprint arXiv:2412.14616*, 2024.

[22] Z. Wu, Z. Peng, and L. Yu, "Fresh2comm: Information freshness optimized collaborative perception," *arXiv preprint arXiv:2502.07852*, 2025.

[23] K. Yang, D. Yang, K. Li, D. Xiao, Z. Shao, P. Sun, and L. Song, "Align before collaborate: Mitigating feature misalignment for robust multi-agent perception," in *Proc. Eur. Conf. Comput. Vis.* Springer, 2024, pp. 282–299.

[24] Y.-C. Liu, J. Tian, N. Glaser, and Z. Kira, "When2com: Multi-Agent Perception via Communication Graph Grouping," in *Proc. IEEE Conf. Comput. Vis. Pattern Recognit.*, 2020, pp. 4106–4115.

[25] A. Rolich, I. Turcanu, A. Vinel, and A. Baiocchi, "Impact of persistence on the age of information in 5G NR-V2X sidelink communications," in *Proc. Medit. Commun. Comput. Netw. Conf.*, 2023, pp. 15–24.

[26] J. Chen, H. Wu, F. Lyu, P. Yang, Q. Li, and X. Shen, "Adaptive resource allocation for diverse safety message transmissions in vehicular networks," *IEEE Trans. Intell. Transp. Syst.*, vol. 23, no. 8, pp. 13 482–13 497, 2022.

[27] F. Lyu, N. Cheng, H. Zhu, H. Zhou, W. Xu, M. Li, and X. Shen, "Towards rear-end collision avoidance: Adaptive beaconing for connected vehicles," *IEEE Trans. Intell. Transp. Syst.*, vol. 22, no. 2, pp. 1248–1263, 2021.

[28] A. H. Lang, S. Vora, H. Caesar, L. Zhou, J. Yang, and O. Beijbom, "Pointpillars: Fast encoders for object detection from point clouds," in *Proc. IEEE/CVF Conf. Comput. Vis. Pattern Recognit.*, 2019, pp. 12 697–12 705.

[29] H. Kim, X. Ma, and B. R. Hamilton, "Tracking low-precision clocks with time-varying drifts using kalman filtering," *IEEE/ACM Trans. Netw.*, vol. 20, no. 1, p. 257–270, Feb. 2012.

[30] G. Hollósi and D. Ficzer, "Adaptive kalman filtering in offset estimation for precision time protocol," *IEEE Trans. Industr. Inform.*, vol. 21, no. 1, pp. 396–404, 2025.

[31] M. Xia, B. Liu, Y. H. Hu, K. Chi, X. Wang, and J. Liu, "PACE: Physically-assisted channel estimation," *IEEE Trans. Wirel. Commun.*, vol. 19, no. 6, pp. 3769–3781, 2020.

[32] S. Lagen, K. Wanuga, H. Elkotby, S. Goyal, N. Patriciello, and L. Giupponi, "New radio physical layer abstraction for system-level simulations of 5G networks," in *Proc. 2020 IEEE Int'l. Conf. Commun.*, 2020, pp. 1–7.

[33] K. Wu, C. Yang, and Z. Li, "Interactionmap: Improving online vectorized hdmap construction with interaction," in *Proc. IEEE Comput. Soc. Conf. Comput. Vis. Pattern Recognit.*, 2025, pp. 17 176–17 186.

[34] S. Bai, J. Z. Kolter, and V. Koltun, "An empirical evaluation of generic convolutional and recurrent networks for sequence modeling," *arXiv preprint arXiv:1803.01271*, 2018.

[35] Q. Han, X. Wang, W. Shen, and Y. Shi, "AdaFML: Adaptive federated meta learning with multi-objectives and context-awareness in dynamic heterogeneous networks," *IEEE Trans. Emerg. Top. Comput. Intell.*, vol. 9, no. 2, pp. 1428–1440, 2025.

[36] Q. Han, X. Wang, and W. Shen, "Hypergraph-aided dynamic model splitting in 6G-enabled collaborative edge computing with meta reinforcement learning," in *Proc. 2025 IEEE Int. Conf. Commun. Workshops*, 2025, pp. 1335–1340.

[37] R. H. Yuan, C. N. Taylor, and S. L. Nykl, "Accurate covariance estimation for pose data from iterative closest point algorithm," *Navig. J. Inst. Navig.*, vol. 70, no. 2, 2023.

[38] S. Chen, B. Liu, C. Feng, C. Vallespi-Gonzalez, and C. Wellington, "3D point cloud processing and learning for autonomous driving: Impacting map creation, localization, and perception," *IEEE Signal Process. Mag.*, vol. 38, no. 1, pp. 68–86, 2021.

[39] Y. Guo, H. Wang, Q. Hu, H. Liu, L. Liu, and M. Bennamoun, "Deep learning for 3D point clouds: A survey," *IEEE Trans. Pattern Anal. Mach. Intell.*, vol. 43, no. 12, pp. 4338–4364, 2020.

[40] D. Krajzewicz, J. Erdmann, M. Behrisch, and L. Bieker, "Recent development and applications of sumo-simulation of urban mobility," *Int. J. Advances Syst. Measurements*, vol. 5, no. 3, 2012.

[41] B. R. Kiran, I. Sobh, V. Talpaert, P. Mannion, A. A. A. Sallab, S. Yoganani, and P. Pérez, "Deep reinforcement learning for autonomous driving: A survey," *IEEE Trans. Intell. Transp. Syst.*, vol. 23, no. 6, pp. 4909–4926, 2022.